

# Three-Dimensional Spatial and Temporal Temperature Control With MR Thermometry-Guided Focused Ultrasound (MRgHIFU)

Charles Mougenot,<sup>1,2</sup> Bruno Quesson,<sup>1</sup> Baudouin Denis de Senneville,<sup>1</sup> Philippe Lourenco de Oliveira,<sup>1</sup> Sara Sprinkhuizen,<sup>3</sup> Jean Palussière,<sup>1</sup> Nicolas Grenier,<sup>1</sup> and Chrit T.W. Moonen<sup>1\*</sup>

**High-intensity focused ultrasound (HIFU) is an efficient noninvasive technique for local heating. Using MRI thermal maps, a proportional, integral, and derivative (PID) automatic temperature control was previously applied at the focal point, or at several points within a plane perpendicular to the beam axis using a multispiral focal point trajectory. This study presents a flexible and rapid method to extend the spatial PID temperature control to three dimensions during each MR dynamic. The temperature in the complete volume is regulated by taking into account the overlap effect of nearby sonication points, which tends to enlarge the heated area along the beam axis. Volumetric temperature control in vitro in gel and in vivo in rabbit leg muscle was shown to provide temperature control with a precision close to that of the temperature MRI measurements. The proposed temperature control ensures heating throughout the volume of interest of up to 1 ml composed of 287 voxels with 95% of the energy deposited within its boundaries and reducing the typical average temperature overshoot to 1°C. Magn Reson Med 61:603–614, 2009. © 2008 Wiley-Liss, Inc.**

**Key words:** MRI; temperature mapping; HIFU; in vivo; feedback control

High-intensity focused ultrasound (HIFU) is an efficient noninvasive technique to produce local heating deep inside the human body (1,2). MRI provides excellent visualization of anatomical structures and tumors for treatment planning (3). In addition, MRI can provide continuous temperature mapping based on the proton resonance frequency (PRF) shift of water with a good spatial and temporal resolution (4,5) for real-time therapy control. New MRI developments in high-field, rapid imaging and magnet field stability have contributed to the performance of MRI temperature mapping. In parallel, major improvement

in ultrasound technology have been made in the field of phased-array MR-compatible transducers (6). These recent developments offer the possibility to treat several points simultaneously and in a minimal amount of time.

Automatic control of the temperature (7) or the thermal dose effect (8) during HIFU heating has been shown to be feasible. Using rapid temperature MRI methods and real-time data processing, an automatic proportional, integral, and derivative (PID) temperature feedback loop has been presented to control the temperature in a single point, the HIFU focal spot (9). This temperature control method has been extended to several points (10) using a multispiral trajectory of the HIFU focal point within a single plane perpendicular to the beam axis. In the latter method, the energy deposition during the next multispiral trajectory is calculated upon completion of the previous one. The resulting volume treated in three dimensions is deduced from numerical simulations. The focal point trajectory remains in a plane perpendicular to the beam axis since the overlap of the acoustic field for each focal point location presents difficulties for volumetric temperature control along the beam axis.

Here, a novel method is proposed for volumetric temperature regulation with temperature control for each voxel of the predefined volume by taking into account beam overlap for the different sonication points. The optimum focal point locations and HIFU intensities are determined following each volumetric temperature map, leading to a rapid and flexible method. The new method was tested in vitro and in vivo using an in-house-designed HIFU phased-array system integrated into a clinical 1.5T MRI system. Due to the phased-array technology, the position and intensity of each sonication could be adjusted every 70 ms. The proposed treatment procedure ensures the treatment of the complete selected volume since the whole volume is heated simultaneously. In addition, the total amount of deposited energy is minimized.

## THEORY

### General Description

The algorithm used to control the temperature  $T(r,t)$  at a time  $t$  at the location  $r$  is based on the general PID temperature control equation:

$$\frac{\partial \xi_{(\vec{r},t)}}{\partial t} + a\xi_{(\vec{r},t)} + \frac{a^2}{4} \int_0^t \xi_{(\vec{r},t)} dt = 0, \xi_{(\vec{r},t)} = \theta_{(\vec{r},t)} - T_{(\vec{r},t)}, \quad [1]$$

<sup>1</sup>Laboratory for Molecular and Functional Imaging: From Physiology to Therapy, UMR5231 Centre National de la Recherche Scientifique (CNRS)/Université "Victor Segalen" Bordeaux 2, Bordeaux, France.

<sup>2</sup>Philips Systèmes Médicaux, Suresnes, France.

<sup>3</sup>Image Sciences Institute, University Medical Center Utrecht, Utrecht, The Netherlands.

\*Correspondence to: C.T.W. Moonen, Imagerie Moléculaire et Fonctionnelle, UMR 5231 CNRS, Université "Victor Segalen" Bordeaux 2, 146 rue Leo Saignat, case 117, 33076 Bordeaux, France. E-mail: chrit.moonen@imf.u-bordeaux2.fr.

Grant sponsor: Ligue National Contre le Cancer, European Union-Network of Excellence "Diagnostic Molecular Imaging" EC-FP6-project; Grant number: LSHB-CT-2005-512146; Grant sponsors: Conseil Régional d'Aquitaine; Cancer Diagnosis and Therapy by Ultrasound (CDTU) Canceropôle Network.

Received 19 January 2008; revised 20 October 2008; accepted 20 October 2008.

DOI 10.1002/mrm.21887

Published online 18 December 2008 in Wiley InterScience (www.interscience.wiley.com).

© 2008 Wiley-Liss, Inc.

where  $\xi_{(r,t)}$  represents the difference between the measured temperature  $T$  and the target temperature  $\theta$ . This second-order differential equation, with a unique double negative root  $-a/2$ , ensures stable convergence between the target and the experimental temperature. It is composed of three terms: 1) the derivative term, which corresponds to the future temperature variation; 2) the proportional term, which corresponds to the present temperature error; and 3) the integral term, which corresponds to the sum over time of the past temperature errors.

The parameter  $a$ , defined by the operator, offers the possibility to adjust the response time (equal to  $2/a$ ) of the feedback loop. The proportional and integral terms are quantified by a comparison between the target temperature and the temperature measured from MR images. The sum of three terms is maintained equal to zero according to Eq. [1] by adjusting the derivative term with the applied HIFU power.

The general PID control algorithm of Eq. [1] can be adapted for MR-guided HIFU temperature control in vivo using the bioheat transfer equation (BHTE), which links the applied power  $P_{(r,t)}$  to the spatial and temporal temperature variation:

$$\frac{\partial T}{\partial t}(\bar{r},t) = D \cdot \nabla^2 T(\bar{r},t) + \alpha \cdot P(\bar{r},t) \quad [2]$$

The BHTE offers the possibility to anticipate tissue temperature effects by taking into account the thermal diffusion effect. The thermal diffusion factor  $D$  is similar for all types of tissue and ranges from 0.12 mm<sup>2</sup>/s to 0.16 mm<sup>2</sup>/s (11). Because the feedback is more stable with an underestimation of the diffusion coefficient (9), it was chosen equal to 0.1 mm<sup>2</sup>/s for all types of tissue used. The ultrasound absorption factor  $\alpha$ , mainly adjusted based on user experience, was set equal to 0.04 K/J<sub>AC</sub> for all experiments. Note that the perfusion term has been removed from the original equation (12) since the experiments were performed in phantoms or tissue with no or low perfusion. The temperature variation induced by eventual perfusion effects is thus compensated for by the proportional and integrative terms of the controller.

According to Eqs. [1] and [2], the power to be applied in a single point in order to perform temperature regulation is defined by the following relation:

$$P(\bar{r},t) = \frac{1}{\alpha} \left[ \frac{\partial \theta(\bar{r},t)}{\partial t} - D \cdot \nabla^2 T(\bar{r},t) + a(\theta(\bar{r},t) - T(\bar{r},t)) + \frac{a^2}{4} \int_t (\theta(\bar{r},t) - T(\bar{r},t)) dt \right] \quad [3]$$

This calculation method thus ensures a stable temperature regulation. Phased-array transducers are capable of producing several regularly spaced focal points simultaneously (13). However, the use of multiple focal points significantly increases the number of side lobes (13) and thus decreases the spatial accuracy. A secure and more flexible method consists of moving the focal point very fast in order to sonicate each point of the volume of interest

(VOI) as frequently as possible. With this approach, the energy  $E(r,t)$  to be deposited during the feedback cycle  $t_F$  is determined by Eq. [4]:

$$E^{PID}(\bar{r},t) = \frac{t_F}{\alpha} \left[ \frac{\partial \theta(\bar{r},t)}{\partial t} - D \cdot \nabla^2 T(\bar{r},t) + a(\theta(\bar{r},t) - T(\bar{r},t)) + \frac{a^2}{4} \int_t (\theta(\bar{r},t) - T(\bar{r},t)) dt \right] \quad [4]$$

This required energy distribution corresponds to the product of the power to be applied during the feedback cycle time  $t_F$ . This duration  $t_F$  should be as short as possible to optimize the quality of the feedback temperature control, but sufficiently long to allow the sonication of a sufficient number of points.

Below, the different steps are described for the calculation of the optimal positions and energies of the different sonication points to be achieved during the next feedback cycle time  $t_F$  for a given hardware setup.

#### Step 1: Calculation of the Required Energy Distribution

Based on the VOI for which the temperature control must be performed, a rapid MR protocol must be determined for volume or multislice temperature mapping covering the complete VOI. Reviews on temperature mapping can be found elsewhere (5,14,15). The dynamic duration of this protocol thus determines the feedback cycle time  $t_F$ . Based on the desired temperature evolution and using Eq. [4], the required energy distribution is calculated for the PID controller with the desired response time, including anticipation of temperature effects based on the BHTE. Since the energy required is now defined in order to reach the target temperature, the next step consists of defining the list of focal points that optimally realize this energy deposition, even in the presence of beam overlap.

#### Step 2: Calculation of the Ideal Sonication Trajectory to Produce the Required Energy Distribution

The simplest approach consists of defining a list in which an equal energy  $E^{PID}(r,t)$  is deposited for each focal point at location  $r$ . However, as described by Fig. 1c and d, when several sonications at different focal points are performed, an energy accumulation occurs systematically, in particular along the beam axis, due to overlap of the acoustic fields of the different sonication points (16). Figure 2a illustrates this effect in one dimension along the beam axis with several focal points with an arbitrary illustrative FWHM of 7.4 mm relative to a 10-mm-square box distribution of energy required. If a sufficient amount of energy is deposited in the central point, superposition of the flanks of the energy deposition curves of neighboring focal points induces a final energy overshoot in the central point. This overshooting becomes even more important in three dimensions when the sonication fields of a large number of focal points overlap.

A standard solution for this type of problem is a deconvolution of the energy required  $E^{PID}(r)$  with the normalized energy distribution deposited by the shape of a single focal

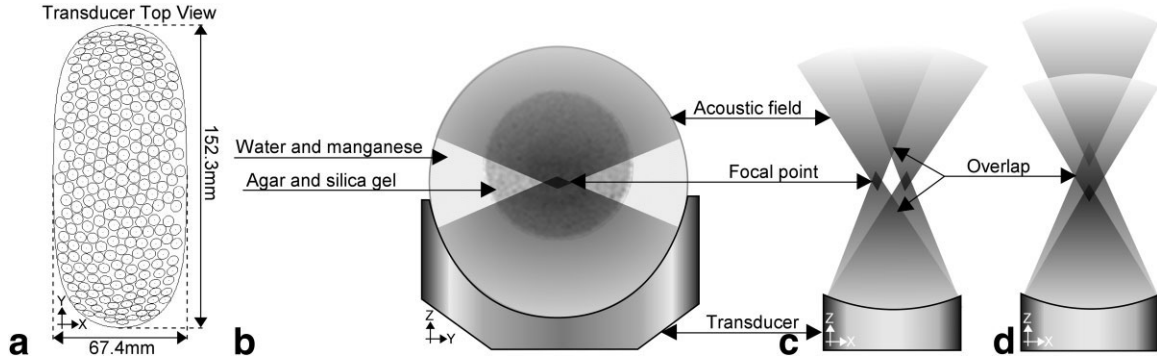


FIG. 1. **a:** Schematic top view of the transducer showing the position of the 256 elements. **b:** Illustration of the transducer and the target gel with a water coupling system. **c,d:** Illustration of the overlap of the acoustic fields from two sonications performed perpendicularly and along the beam axis, respectively.

point  $FP^{1pt}(r)$ . However, this method, which includes a zero value for the energy required outside of the target volume, is not appropriate because it leads to a list of points with negative intensity value, which is physically impossible.

The proposed new solution is illustrated in a simplified way in Fig. 2b. The idea is to minimize the total energy required to produce the desired spatial energy distribution in the VOI. Such a result can be obtained based on the detection of the maximum of the remaining differential energy for each voxel. The remaining differential energy is defined here as the difference between the energy required by the tissue for

temperature control according to Eq. [4] and the energy produced by the focal point trajectory during the  $n^{\text{th}}$  iteration. The following convenient iterative algorithm can be used to calculate this ideal sonication trajectory:

$$E_{(\vec{r})}^0 = E_{(\vec{r})}^{PID} \text{ and } L_{(\vec{r})}^0 = 0$$

Point  $\vec{r}_n$  corresponds to the maximum defined by

$$\begin{aligned} E_{(\vec{r}_n)}^n &= \max(E_{(\vec{r})}^n) \\ L_{(\vec{r})}^{n+1} &= L_{(\vec{r})}^n + R \cdot E_{(\vec{r}_n)}^n \cdot \delta_{(\vec{r}-\vec{r}_n)} \\ E_{(\vec{r})}^{n+1} &= E_{(\vec{r})}^n - R \cdot E_{(\vec{r}_n)}^n \cdot FP^{1pt}_{(\vec{r}-\vec{r}_n)} \end{aligned} \quad [5]$$

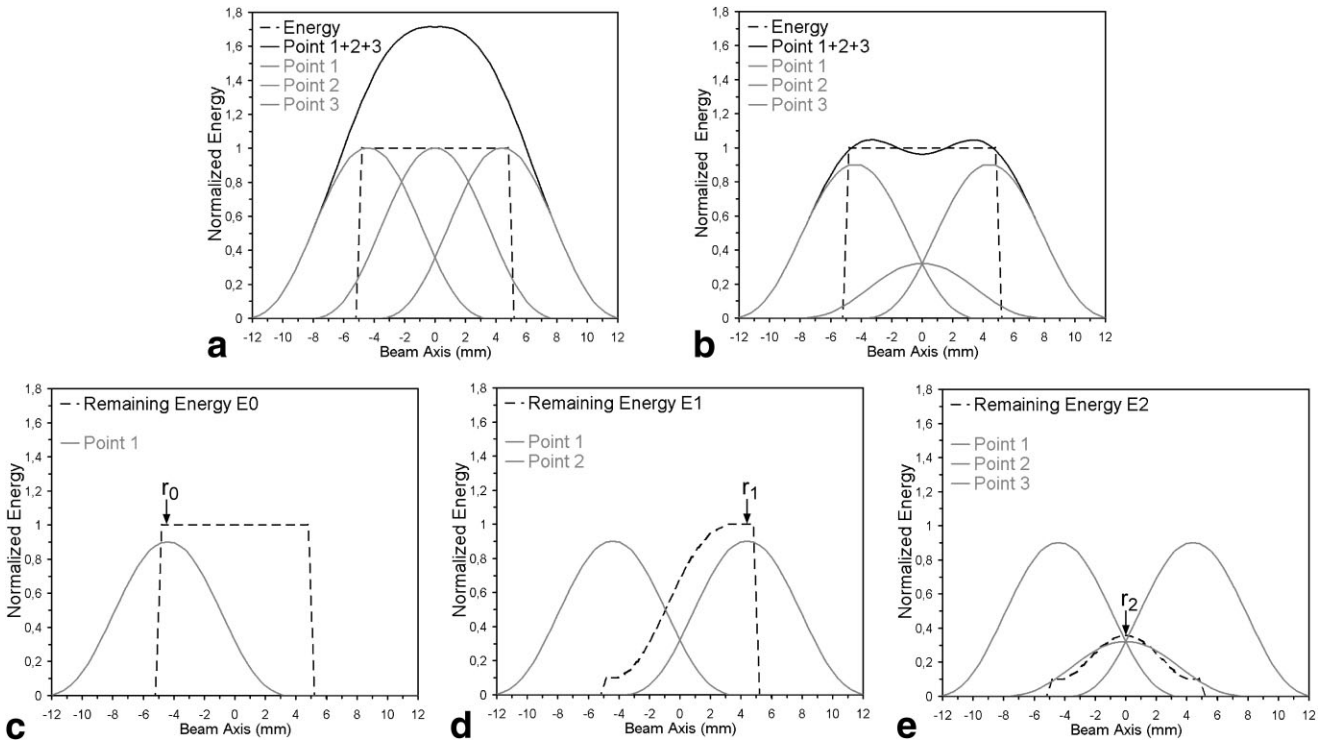


FIG. 2. **a:** Illustration of the beam overlap effect in one dimension in the case of a list of focal points directly deduced from the required energy (not taking into account any beam overlap). **b:** Reduction of the effect of beam overlap when using a list of sonication points deduced with an iterative algorithm in which focal points are proportional to the maximum remaining energy according to one (c), two (d), and three (e) iterations.

The energy distribution produced by a single focal point  $FP^{1st}$  is deduced from a simulation of the acoustical field produced by the phased-array transducer based on Rayleigh integration. In Eq. [5],  $\delta(r)$  represents a Dirac function that is equal to one for  $r = 0$ , and zero in all other cases. The point  $r_n$  represents the location of the maximum of the remaining differential energy  $E^n$  in order to construct the list of points function  $L^n$ , which is a sum of translated Dirac function with a ratio  $R \cdot E^n(r_n)$ . The ratio  $R$  is further explained below.

Initially, the remaining differential energy  $E^0$  corresponds to the energy defined by the PID controller  $E^{PID}$ , whereas the list of points  $L^0$  does not include any focal point. The location of the first focal point  $r_0$  to be performed corresponds to a maximum of the remaining differential energy  $E^0$ . In the case of initial homogenous energy distribution as described in Fig. 2c, it might correspond to any maximum, such as an edge point of the targeted volume. The intensity of this first focal point of the list  $L^1$  is set equal to a ratio  $R$  of the maximum of the detected remaining differential energy. This ratio should thus be set to a value lower than one in order to avoid an overshoot due to a superposition of the flanks of neighboring focal points. To prepare the next iteration step, the remaining differential energy  $E^1$  is defined by subtracting the energy to be deposited at the location  $r_0$  from  $E_0$ . The second iteration (see Fig. 2d) consists of defining a second focal point  $r_1$  located at the maximum of the remaining differential energy  $E^1$  with an intensity equal to a ratio  $R$  of this maximum value. In a similar way, the third focal point (see Fig. 2e) corresponds to a ratio  $R$  of the remaining differential energy  $E^2$ . This method is iteratively repeated to determine the energy to be applied in each focal point of the trajectory. Note that the final focal point trajectory is thus automatically optimized in the presence of beam overlap.

The required number of iterations to reach the target temperature depends on the value of  $R$ . For a value of  $R$  close to one, only a limited number of iterations are required (see Fig. 2 with three iterations for  $R$  equal to 0.9). However, with such a limited number of control points, the risk of overshoot increases (for example, if the first point is inadvertently chosen in the middle of the region). On the contrary, a very low value of  $R$  will require a large number of iterations. In practice, this ratio  $R$  was chosen equal to 0.1 to avoid overshooting. For a target area that includes  $N$  voxels under control, the remaining differential energy  $E^n$  is reduced at least by a factor  $1-R$  after  $N$  iteration as described by the comparison:

$$\max(E_{(r)}^{n+N}) \leq (1 - R) \cdot \max(E_{(r)}^n). \quad [6]$$

As a consequence, the ratio  $R$  ensures a geometric convergence of the remaining differential energy to zero. However, complete convergence is never reached because the maximum of the remaining differential energy approaches zero with a ratio  $1 - R$  of the preceding remaining differential equation. For this reason, iterations are stopped when the maximum of the remaining differential energy corresponds to a percentage equal to 2% of the initial maximum energy required. This algorithm, optimized for a

calculation of energy values of voxels of the target region only, typically takes less than 10 ms for 200 voxels using a 3 GHz processor.

### *Step 3: Calculation of the Sonication Trajectory To Be Realized With Given Hardware and Software Limitations*

Following the ideal trajectory calculation of step 1, the resulting list function is converted into a limited list of sonication points by first removing all null values. If the number of points of the remaining list exceeds the maximum number of focal points that can be sonicated within the feedback duration  $t_F$ , focal points with the lowest assigned energy to be deposited are removed.

In the examples presented in this study, this case did not occur frequently, since the system used allowed sonication of 34 points within the feedback cycle time of 2.4 s. In addition, the list function usually obtained corresponded to a shape in which most sonications to be performed were located at the edge of the volume and, for a volume with rectangular shapes, predominantly at the corners.

Finally, to avoid sonication with a very high power intensity, potentially producing cavitation effects (17), the energy deposited by each point of the list is mainly adjusted by the duration of sonication. The resulting applied power is thus the same for each point of the list. Only for points with very small energy deposition, for which the duration of sonication could not be reduced below the HIFU system driver update time (70 ms for the system used), the deposited energy was adjusted by decreasing the power. For all experiments, the acoustical power was limited to 50 W<sub>AC</sub> in order to stay below the cavitation threshold.

According to the algorithms described above in steps 1–3, up to 34 focal points positions (within the target volume), together with their associated power and duration, are redefined dynamically following acquisition of each new set of thermal maps. The resulting energy distribution ensures the deposition of the energy required in the target volume with a minimal amount of total energy since only locations corresponding to a maximum of required energy are sonicated. However, some energy is deposited outside of the target region due to the size of the focal point (full-width at half-maximum of the focal point's intensity in this study:  $0.48 \times 1.28 \times 1.6$  mm<sup>3</sup>) and in a more predominant way due to secondary lobes along the beam path. For the same reasons, energy distributions with steep gradients may not be performed.

## **MATERIALS AND METHODS**

### **MRI-Guided HIFU Platform**

Experiments were performed with a Philips 1.5T Intera clinical scanner (Philips Medical Systems, Best, The Netherlands) with a single loop receiver coil (16 cm diameter). Inside this magnet was an ultrasound platform designed to treat breast tumors (18). The position of the transducer is mechanically adjusted by knobs located at the foot of the MR platform bed (TSR SA, Merignac, France).

The focal length of this transducer operating at 1.5 MHz was 80 mm. This transducer, manufactured by Imasonic SA (Besançon, France), was designed to be elliptical on the



side view (plane XZ on Fig. 1) to facilitate rotational displacement around the Y-axis. As a consequence, the beam presents a large aperture angle of  $144^\circ$  in the horizontal plane (152.3 mm large diameter) and a smaller aperture angle of  $50^\circ$  in the vertical plane (67.4 mm small diameter), as described in Fig. 1. This elongated transducer geometry allows a beam axis to be included in the horizontal plane. The active surface of this phased-array transducer is composed of 256 elements of 5.8 mm diameter, arranged in an asymmetrical and compact distribution.

The coupling between skin (or gel) and piezo elements of the transducer was provided by circulating degassed water. The water was previously degassed for several days at 25 mBar with a membrane vacuum pump (Ilmvac GmbH, Thüringen, Germany) and installed in an immersion system connected on the front face of the transducer just before the beginning of the experiments. The temperature of the water was regulated at  $10^\circ\text{C}$  for gel experiments and  $20^\circ\text{C}$  for in vivo experiments on rabbit muscle, in order to cool down the active surface of the transducer. To avoid motion artifacts induced by the displacement of the degassed water, 1 g/liter of manganese chloride (Sigma-Aldrich, St. Louis, MO, USA) was added to completely eliminate the MR signal of circulating water under the conditions of the temperature MRI measurements.

A dedicated 256-channel amplifier (RCDC SA, St. Martin de Hinx, France; TDM SA, Merignac, France), controlled by a personal computer with an update time of 70 ms, was used to drive the 256 channels of the phased-array transducer.

### Temperature MRI Sequences

MR thermal images were obtained using an RF-spoiled gradient-echo sequence (echo-planar imaging [EPI] factor = 11, TE = 18 ms, TR = 300 ms, flip angle =  $35^\circ$ , and bandwidth = 30.1 Hz). Thermal maps were computed based on PRF principles from phase variation using temporal phase unwrapping. The initial phase used as a reference was averaged over the first four acquired dynamics to improve temperature precision. To compensate for temporal instability of the main magnetic field (19), also referred to as baseline drift, a first-order compensation was performed by subtracting the spatially averaged apparent temperature of nonheated regions selected by the user. For phantom studies, the field of view (FOV) was  $128 \times 128 \text{ mm}^2$ . For in vivo studies, the FOV was  $140 \times 140 \text{ mm}^2$  and outer volume suppression was included to reduce respiratory motion artifacts. Other parameters were identical for both cases. Six horizontal slices of 4 mm thickness with spacing between slices of 0.4 mm were acquired every 2.4 s. The acquired matrix of  $96 \times 96$  was reconstructed to a  $128 \times 128$  matrix in order to obtain an apparent resolution of  $1 \times 1 \times 4 \text{ mm}^3$  for phantom studies and  $1.09 \times 1.09 \times 4 \text{ mm}^3$  for in vivo studies.

In this study, the central slice included the beam axis. In addition, slices orientation was chosen to include the larger aperture angle of the transducer in order to show almost all of the near field and the far field within a single slice. As a consequence, this slice orientation includes almost the complete acoustic field (beam aperture of  $144^\circ$  within the slice and  $50^\circ$  perpendicularly to the slice) and

shows the largest number of voxels heated by the overlap effect of different beam paths occurring mainly within the central slice.

### In Vitro MR-Guided HIFU Studies

The automatic volumetric heating procedure was initially tested in vitro with an agar gel of 8.5 cm diameter composed of 2% of agar (Invitrogen, CA, USA) and 1% of silica (Sigma-Aldrich) in order to simulate the absorption of the ultrasound waves in biological tissue.

Using the available HIFU and MRI system, volumetric temperature data were updated every 2.4 s (setting  $t_F$  also to this value), allowing us to sonicate 34 points during  $t_F$  with 70 ms for every sonication point. The response time  $2/a$  (Eq. [1]) of the PID feedback loop was set to 15 s in order to be several times larger than the latency time of the data acquisition, transfer, and analysis.

To demonstrate that the feedback temperature can produce variable spatial heating patterns with different levels and durations of temperature increases, 24 heating were performed in vitro. As described in Table 1, the target temperature increase ranged from  $10^\circ\text{C}$  to  $20^\circ\text{C}$ , starting with a sinusoidal slope ranging from 60 s to 180 s, followed by a plateau with a duration ranging from 60 s to 120 s. Therefore, the total time of the temperature control (sinusoidal slope and plateau) ranged from 140 s to 320 s. The temperature controls were performed for a line of voxels with total length of 13 mm (eight cases), a cube of 7 mm width (four cases), a sphere of 12 mm diameter (11 cases), or a large sphere of 15 mm diameter (one case). The typical case of a spherical volume and the particular case of a linear volume are described below in more detail to illustrate the feedback temperature controller performance. The size of the target volumes were chosen to respect the maximal electronic focal point steering allowed by this transducer ( $-13.73 \text{ mm}$  to  $+11.45 \text{ mm}$  along the beam Z-axis,  $\pm 7.31 \text{ mm}$  along the X-axis, and  $\pm 8.52 \text{ mm}$  along the Y-axis, as indicated in Fig. 1). The center of the target volumes was located at a depth of 30–40 mm inside the phantom. Two nonheated regions located outside of the ultrasound beam path were used to correct the average baseline drift. These regions included approximately 700 voxels selected in each slice on the left and right sides of the beam path.

### In Vivo MR-Guided HIFU Studies

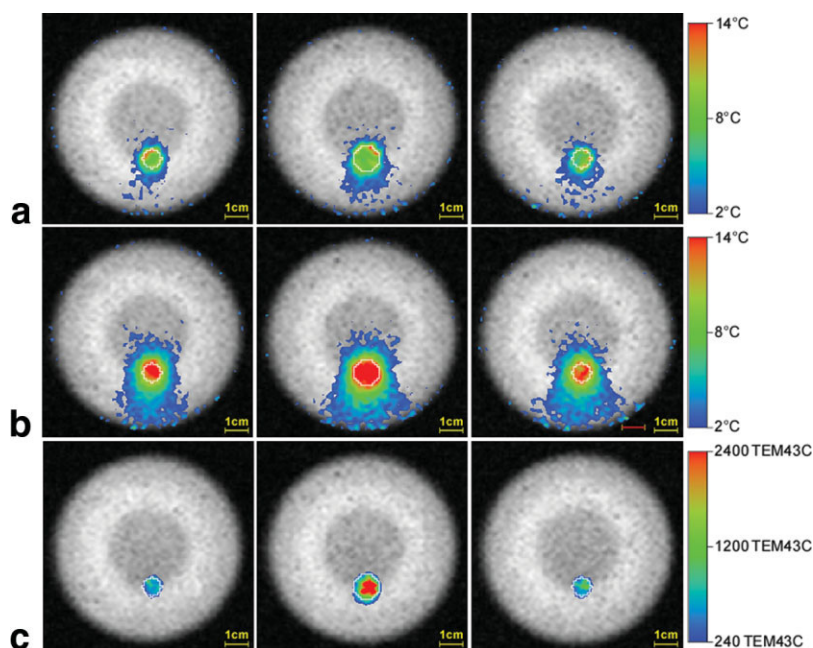
In vivo studies were performed on rabbit leg muscle in accordance with French laws governing the care and the use of animals for research. Four rabbits of 3 kg were used to produce thermal ablation in the leg muscle. The animals were initially anesthetized with a premedication of 0.5 ml intramuscular injection of Zolazepam (Zoletil, Virbac S.A., Carros, France). One leg was shaved and the remaining hair was removed using hair removal cream (Crème Dépilatoire, Casino, France). The anesthesia was maintained during experiment with 2% isoflurane (AErrane, Baxter S.A., Maurepas, France) in 98% air ventilated via an adapted mask, leading to approximately one respiratory cycle per second. In addition, 0.5 ml of the analgesic tolfenamic acid (Tolfedine, Vetoquinol S.A., Lure, France)

Table 1  
List of Volumetric Heating Episodes Performed and Summary of Results

Volume geometry	Medium										
	Target parameters			Number of voxels heated <sup>a</sup>		Temporal temperature analysis				Acoustic energy	
	Target temperature increase (°C)	Plateau duration (s)	Total time (s)	Number of voxels of the volume	Inside the target volume	Outside the target volume	Average max-min <sup>b</sup> (°C)	Average overshoot <sup>c</sup> (°C)	SD overshoot <sup>d</sup> (°C)	Total emit (KJ <sub>ac</sub> )	At the border (%)
Phantom (2% agar and 2% silica) Line 13 mm	10	80	140	13	12	63	2.05	0.15	0.64	2.03	100
	10	80	140	13	13	65	2.19	0.25	0.64	2.05	100
	15	100	200	13	13	71	2.18	-0.04	0.28	4.55	100
	15	100	200	13	13	61	2.47	0.04	0.45	4.19	100
	15	100	180	13	13	78	3.07	-0.07	0.48	3.03	100
Cube 7 mm	15	100	180	13	13	131	3.45	-0.11	0.61	3.47	100
	15	100	180	13	12	63	3.49	-0.1	0.64	3.48	100
	15	100	180	13	13	187	3.74	0.06	0.58	1.68	100
	10	80	140	147	147	116	4.46	0.87	0.95	2.62	95.63
	10	80	140	147	145	93	5.21	0.97	1.2	2.82	93.75
Sphere 12 mm diameter	14	100	200	147	147	214	5.01	0.87	1.08	5.87	96.34
	14	100	200	147	147	79	5.45	0.67	0.76	4.82	95.65
	10	80	140	195	193	126	5.25	1.03	1.08	2.91	90.96
	10	80	140	195	195	188	5.15	0.84	1.08	3.12	88.53
	12	120	220	195	194	93	6.85	0.93	1.02	2.94	92.87
Sphere 15 mm diameter	12	120	220	195	195	85	7.14	0.87	1.01	3.07	90.04
	14	100	200	195	195	263	5.21	0.94	1.55	5.71	90.79
	14	100	200	195	194	98	5.67	0.88	0.94	4.84	89.63
	14	100	200	195	195	135	6.39	1.1	1.19	5.32	89.89
	14	100	200	195	193	150	8.85	1.46	1.76	3.33	94.57
Rabbit in vivo	14	100	180	195	187	41	6.87	0.79	0.96	3.62	94.64
	14	100	180	195	191	51	7.05	0.79	1.29	4.04	90.09
	20	60	240	195	191	37	6.47	0.67	0.8	5.31	95.38
	20	60	240	287	283	50	6.34	0.92	1.06	4.41	95.53
	13	160	320	48	48	54	8.94	1.63	1.75	2.56	95.63
Manually drawn	20	60	240	195	195	376	10.24	2.37	2.56	3.72	87.79
Sphere 12 mm diameter	20	60	240	287	286	468	9.55	2.1	2.35	4.31	82.02
Sphere 15 mm diameter											

<sup>a</sup>Number of voxels reaching the target temperature during more than 20% of the plateau duration.  
<sup>b</sup>Temporal average of the difference between the maximum and the minimum temperature detected inside of the target volume at each dynamic.  
<sup>c</sup>Temporal average of the difference between the mean temperature within the target volume and the target temperature.  
<sup>d</sup>Temporal SD of the difference between the mean of the temperature within the target volume and the target temperature.

FIG. 3. MR temperature maps of three adjacent slices of a gel acquired at time 62 s (a) and 100 s (b), and the final thermal dose maps (c) obtained at 240 s with regulation of a temperature increase of 14°C for 195 voxels located within a spherical volume of 12 mm diameter.



was injected intramuscularly a few minutes before applying HIFU. The body temperature was monitored with an optical fiber (Luxtron Corp., Santa Clara, CA, USA) inserted in the nonheated part of the subcutaneous muscle. After completion of the thermal ablation procedure, the animals were immediately euthanized by an intravenous lethal dose of pentobarbital (Ceva Santé Animale, Libourne, France).

To illustrate the flexibility of the volumetric heating method, an arbitrary target volume (white contour in Fig. 7a) including 48 voxels was initially selected with a drawing tool on the central slice. Two other *in vivo* studies were carried out to demonstrate the ability to heat large, spherical target volumes of 12 mm and 15 mm diameter with a target temperature increase set to 20°C. Results for a fourth rabbit are not reported because the temperature

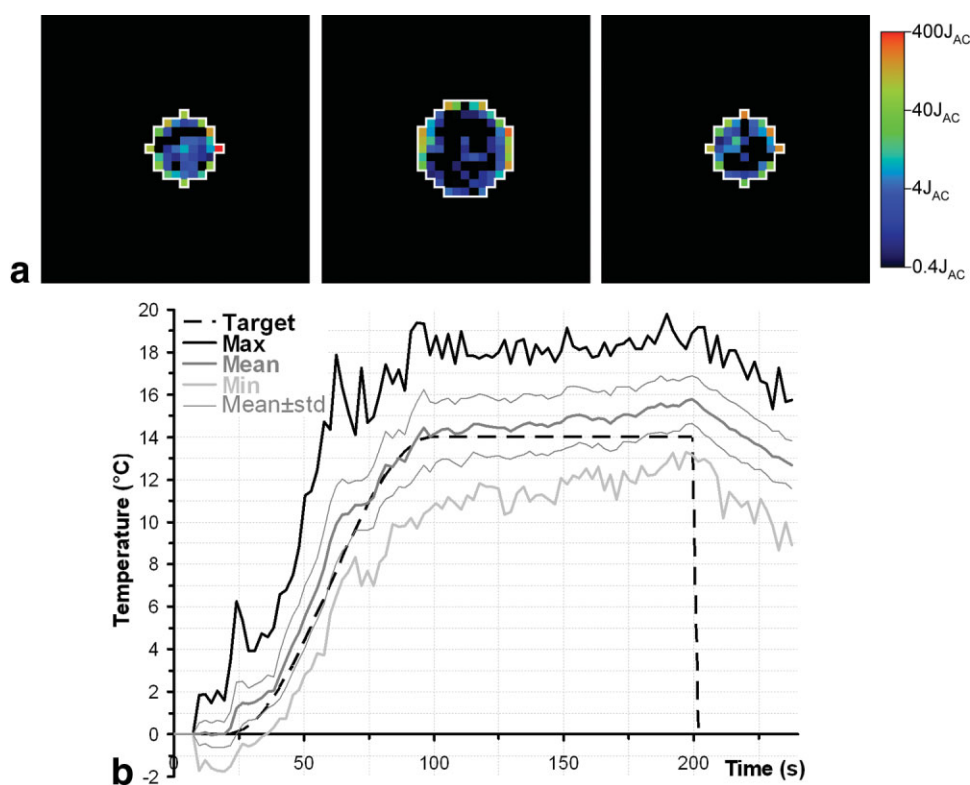


FIG. 4. **a:** Distribution of the total acoustical energy of sonication points in the three adjacent slices shown in Fig. 3 within a spherical volume of 12 mm in diameter, demonstrating that nearly all sonication points were located at the volume edge. **b:** Temporal analysis of the temperature control with the minimum, mean, and maximum temperature of 195 voxels regulated at 14°C during 100 s.

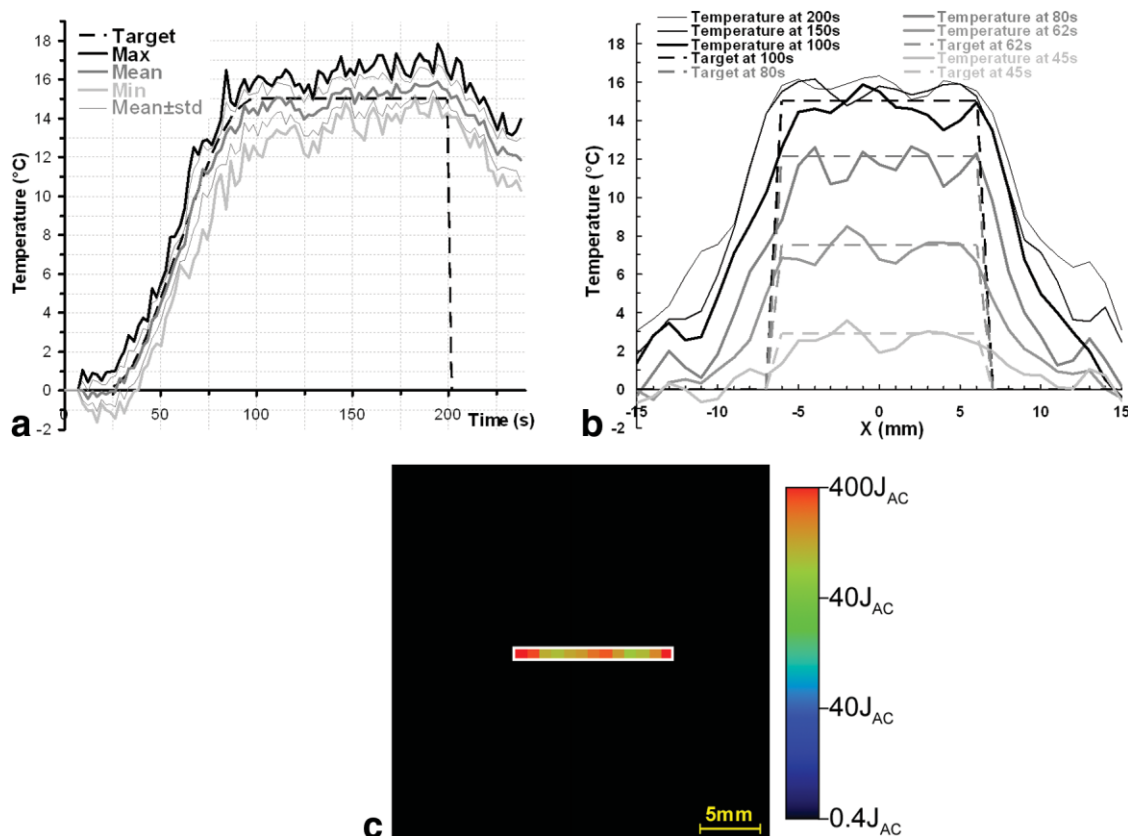


FIG. 5. **a**: Temporal analysis of the temperature control with the minimum, mean, and maximum temperature of a line of 13 voxels regulated at 15°C during 100 s. **b**: Spatial analysis of the temperature increase at time 45 s, 62 s, 80 s, 100 s, 150 s, and 200 s produced along the 13 voxels. **c**: Distribution of the total acoustical energy of sonication points performed within the 13 voxels.

control was automatically interrupted due to a sudden displacement. The center of the target volumes was located at a depth from the skin of 20–30 mm due to the limited muscle volume. For in vivo studies, nonheated

regions for baseline drift correction were selected on the right of the target region and in the middle of the nonheated leg. In addition, these nonheated regions were used to verify the stability of the temperature standard devia-

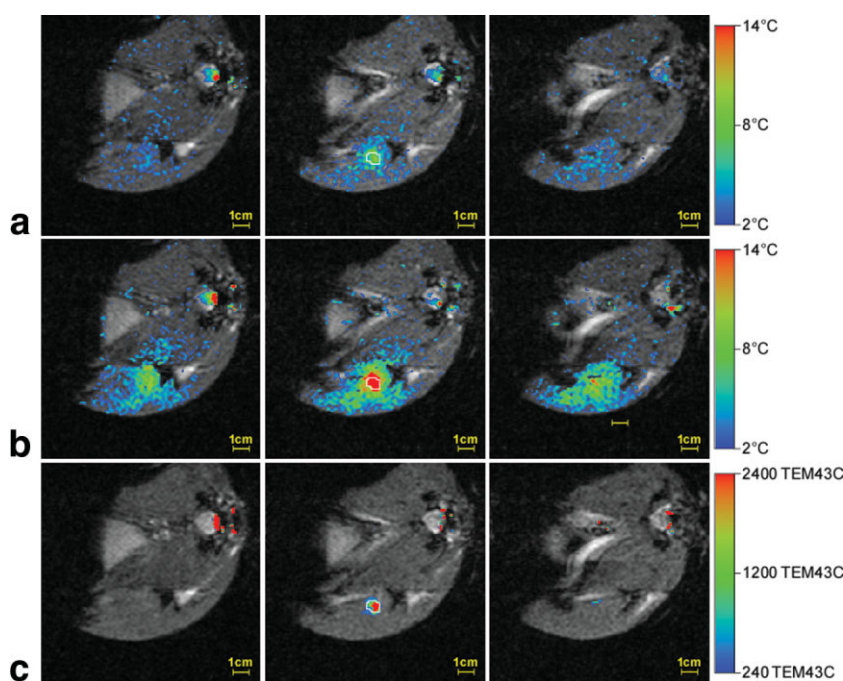
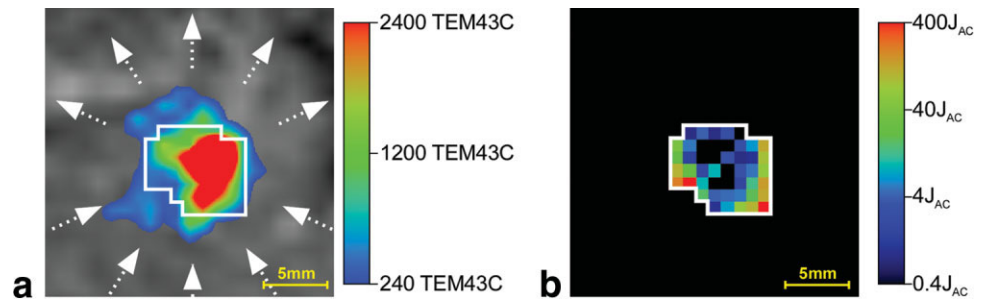


FIG. 6. Thermal maps of three adjacent slices acquired at time 100 s (**a**) and 170 s (**b**), and the final thermal dose map (540 s) (**c**) with a regulation at 13°C of 48 voxels.



FIG. 7. Comparison between the initial selected target region (white contour) and the final thermal dose (color level) (a) and the distribution of the total acoustical energy of sonication points (b).



tion (SD) in order to interrupt the heating in case of adverse events, such as tissue displacement.

## RESULTS

Volumetric temperature regulation is demonstrated for varying target volumes and shapes. Table 1 shows a quantitative summary of results obtained for in vitro and in vivo experiments, together with analyses of the spatial and temporal accuracy of the feedback temperature controller. It can be seen that, in general, all voxels of the target volume reached the required temperature with little or no overshoot. A more detailed analysis of the spatial homogeneity and temporal stability of heating, as well as the required acoustic energy, is provided below.

As a consequence of preselected target parameters (medium, shape, size, temperature increase, and duration), and as a result of beam shape and overlap, some heating occurred outside the target region. In order to quantify heating outside the target region relative to the target region, the number of voxels heated inside and outside of the target volume was quantified as the number of voxels surpassing the value of the target temperature during more than 20% of the plateau duration. The number of voxels heated outside the target volume should be compared with the total number of voxels of the target volume: 13 for a line of 13 mm, 147 for a cube of 7 mm width, 195 for a sphere of 12 mm diameter, 287 for a large sphere of 15 mm diameter, and 48 voxels for the manually drawn volume.

Other parameters, such as the thermal dose threshold set equivalent to 240 min at 43°C (TEM43C), might be used to quantify the number of heated voxels. However, the exponential behavior of thermal dose relatively to the temperature provides very low or very high values (ranging from 21 to 16,000 TEM43C) for relatively low or high target temperature increase values tested (ranging from 10°C to 20°C). The comparison with the target temperature increase provides a direct comparison with the parameter under control: the temperature. We chose the threshold of heating at the target temperature during 20% of the plateau duration as a performance indicator. Other threshold values might be used. Note that a perfectly regulated voxel at the target temperature would, on average, reach a higher temperature during 50% of the plateau duration and a lower temperature also during 50% because of the noise in the temperature maps. A low-duration threshold would indicate that all voxels inside the target volume surpass the target temperature at least during few dynamics, which is less relevant due to the large number of dynamics and

limited SNR. With long durations, voxels inside the target volume may not surpass the target temperature, mostly because of the underestimation due to the limited SNR. As a consequence, the threshold value of 20% of the plateau duration was considered to be a good compromise.

In addition to this spatial temperature analysis, Table 1 provides a temporal analysis with voxel temperatures measured within the target volume. The first value, average max-min, corresponds to the temporal average of the difference between the maximum and minimum temperatures measured within the target volume. The second value, average overshoot, indicates the temporal average of the difference between the mean temperature (within the target volume) and the target temperature. The third value, std overshoot, is the temporal SD of the difference between the mean temperature and the target temperature. Since for the calculation of the std overshoot the value of the average overshoot value is not subtracted, the std overshoot is systematically higher than the average overshoot.

Finally, the total acoustic energy emission for feedback temperature control is provided to estimate the heating efficiency. The relative amount of acoustic energy emission for focal points located within the border of the target volume summarizes the efficiency of the spatial energy distribution.

## In Vitro Experiments

For the 24 experiments performed in vitro, almost all voxels (typically 99%) inside the target volume surpass the target temperature during 20% of the plateau duration, and all voxels (exactly 100%) surpass the target temperature, at least during few dynamics. Together with the target volume, many voxels around the target volume also surpass the target temperature. These voxels are mainly located around the target volume and especially along the beam axis. The ratio of voxels heated outside the target volume to voxels inside depends mainly on the shape of this volume. An elongated shape perpendicular to the beam axis, like a line of voxels, presents a typical ratio of 690%, a cubic shape presents a typical ratio of 85%, and a spherical shape presents a ratio of 56%.

Figure 3a and b illustrate the heating produced with three horizontal adjacent thermal maps, including the beam axis and the spherical target region of the 12 mm diameter at the middle (time 62 s) and the end (time 100 s) of the target temperature rise. To quantify the efficiency of this heating procedure, the final thermal dose in the central slice obtained after the cool-down of the temperature

(time 240 s) is displayed in Fig. 3c, supposing that the initial temperature of the gel is equal to 37°C. The thermal dose scale starts at 240 thermal equivalent minutes at 43°C (TEM43C), which corresponds to an irreversible lethal dose for cells (20,21). As compared to the selected target region indicated by a white contour in Fig. 3, the volume with a lethal thermal dose corresponds to a volume that is nearly spherical with 12 mm width by 14 mm length in the central slice and 8 mm width by 10 mm length in the two adjacent slices. Slices located outside of the acoustic field did not display any significant thermal dose with a temperature variation lower than 8°C. During this experiment a baseline drift of 0.96°C/min was detected and corrected.

The total acoustic energy used to produce the heating increased with the value of the target temperature increase and the plateau duration. However, the number of voxels within the target volume did not significantly impact the total acoustic energy. Most of this acoustic energy emission was located at the border of target volume with typically 93% for cubic and spherical volumes. The central part of the target volume was thus indirectly heated by overlap effect of each ultrasound beam path. The total energy distribution used during the feedback temperature control (presented in Fig. 3) is shown in Fig. 4a. A logarithmic scale is used due to the strong disparity of energy values between the voxels. Most of the sonication points were located at the border of the spherical volume. Only a few percent of sonications are located inside this volume, and those were performed at the onset of the heating procedure.

For the particular case of a linear volume, all 13 voxels under control correspond to border voxels. However, as shown in Fig. 5c with the acoustic energy distribution for a linear volumetric heating, most of the acoustic energy was deposited in corners: the two extremities of the planned target line indicated by a white contour. This particularity, that corners required more acoustic energy, was also systematically noticed for all cubic volumetric heating episodes.

The temporal analysis of the temperature within the linear volume indicates a very good temperature accuracy. The typical average max-min was equal to 2.8°C for linear volume, 5°C for cubic volume, and 6.4°C for spherical volume. The typical average overshoot was negligible for linear volumes (0.02°C) but became significant for cubic and spherical volumes (0.9°C).

As an example, the temporal graph of the spherical target volume (Fig. 4b) shows the minimum, mean ( $\pm$ SD), and maximum temperatures observed over the 195 voxels under control. The average temperature of this spherical volume was initially very close to the target temperature and progressively tended to surpass the target temperature. There was a small temperature overshoot at the center of the volume, especially during the end of temperature regulation, despite the fact that all sonications were performed only at the border.

On the contrary, linear volumes, including small volumes, did not produced any overshoot. As shown for a linear volumetric heating with a spatial and a temporal temperature graph, the 13 voxels under control stayed very close to the target temperature until the end of the heating. Since there was no temperature overshoot in the central

region, the spatial temperature homogeneity within this region was equal to 0.8°C, which was very close to the temperature measurement accuracy of 0.6°C measured before the heating in the same region.

### In Vivo Experiments

The automatic three-dimensional temperature control in vivo represented a higher challenge due to tissue interface, motion artifacts, and the lower temperature measurement accuracy equal to 1.4°C in leg muscle tissue. The body temperature measured with optical sensor indicated values around 37°C decreasing linearly with a slope ranging from  $-2.8^{\circ}\text{C}$  to  $-1.1^{\circ}\text{C}$  per hour, which is negligible relative to the heating duration of few minutes. The baseline drift measured in nonheated regions was almost the same for each slice, ranging from  $-2.5^{\circ}\text{C}$  to  $0.5^{\circ}\text{C}$  during the heating procedure.

Similarly to phantom experiments, all voxels inside the target volume reached the target temperature. However, the number of voxels that surpassed the target temperature outside of the target volume was significantly increased, probably due to the higher noise level and motion artifacts.

The target volume was heated homogeneously according to the target temperature with a typical average min-max equal to 9.6°C. In the same way as for experiments in vitro, central voxels were slightly overheated with a typical average overshoot of 2°C, which is relatively low compared to the target temperature of 20°C.

To illustrate those results, Fig. 6a and b show three adjacent thermal maps obtained at the middle (time 100 s) and the end (time 170 s) of the temperature rise for a manually selected volume of 48 voxels, indicated by a white contour. By approximating the body reference temperature to 37°C, the resulting final thermal dose (at 540 s) is displayed in Fig. 6c. The necrosis produced (according to the thermal dose threshold) is predominantly localized in the central slice relative to the initially selected region except for a region near the rectum for which the temperature maps showed artifacts induced by gas. Figure 7a shows more precisely the correspondence between this target region, defined by the white contour, and the final thermal dose (also presented in Fig. 6c). The initially selected target volume completely reached the lethal dose according to the target temperature (13°C during 160 s), which corresponds to a lethal dose close to 240 TEM43C. Neighboring voxels located in the beam path (indicated by white dot arrows in Fig. 7a) of the acoustic field also reached the target temperature and the lethal dose simultaneously to the target volume.

The temporal analysis of the temperature curves for this in vivo experiment, shown in Fig. 8, indicates that the mean temperature stayed close to the target temperature with a small constant overshoot equal to 1.6°C. Despite the fact that most sonications were located at the border of the target region (Fig. 7b), this overshoot was still located at the center of the heated region, resulting in a larger thermal dose value at this location.

After each in vivo experiment, necrosis was observed with either contrast-enhanced imaging or by macroscopic histology analysis. No skin burns were observed despite the fact that the border of the target sphere was located only 10 mm from the skin.

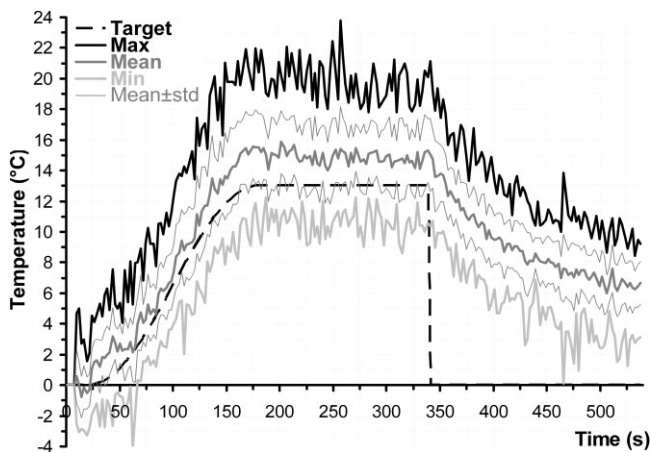


FIG. 8. Temporal analysis of the temperature control with the minimum, mean, and maximum temperature of 48 voxels regulated at 13°C during 100 s.

## DISCUSSION

The proposed volumetric temperature regulation is based on PID control over all sonication points. The location and deposited energy are modified following each acquired temperature map. The method showed excellent performance *in vitro* and *in vivo*, ensuring an adequate temperature increase in the entire VOI. The approach takes advantage of all acquired temperature data since the temperature of each voxel of the heated region is regulated simultaneously during each acquisition of volumetric temperature MRI.

The proposed method is flexible and efficient since in principle any shape of target region can be selected and the corresponding temperature increase will be finally obtained in this region. However, depending on the orientation of the length of the selected region relatively to the beam axis, some neighboring areas might also reach the target temperature in regions along the beam axis. This is a direct consequence of the technical limitation imposed by acoustic field overlap. For this reason, ellipsoidal target regions elongated along the beam axis are more secure because the number of voxels heated outside of the volume under control is significantly reduced.

During feedback temperature control of a large number of voxels, a small overshoot of a few degrees was generally observed at the center of the heating region despite the fact that most sonications were performed at the border. This unwanted effect is related to the absence of heat diffusion from the center (no temperature gradients) and continuing low heating due to the HIFU energy distribution when sonications were performed at some distance. As a consequence, it may be argued that only voxels located at the border of the target region were under effective temperature control. This central overshooting imposed by the impossibility to cool down may not represent a real issue for tumor thermal ablation since it does not represent extra energy cost and does not exceed a few degrees in all performed studies. Despite this central moderate overshooting, the temporal analysis of temperatures within all voxels included into the selected region is in good agree-

ment with the temporal target temperature distribution. The reduction of the number of voxels under control, e.g., a linear volume of 13 voxels, avoids the overshoot effect and offers the possibility to improve the accuracy of the temperature control with homogeneity very close to the noise measurement level.

The proposed method reduces the heating duration of a volume from typically 15 min with the previous multi-spiral method (10) to only 2 min. As a consequence, the diffusion effect is significantly reduced and the spatial temperature slope at the border of the volume heated is improved from 1°C/mm for mechanical spiral trajectories to 3°C/mm (perpendicularly to the beam axis) with fast electronic displacement of the focal point. In addition, the temperature homogeneity is also significantly improved since the temperature is regulated every dynamic (2.4 s) over the complete volume instead of every 2 min within one focal plane.

The proposed approach provides the minimum energy required to produce the temperature increase (deposited primarily at the border and almost nothing inside) of the selected volume. According to the maximum detection algorithm, any removal of a focal point of a trajectory would produce a underheating at the corresponding location inside the target volume. Of course, this heating procedure still requires a judicious selection of target parameters (size, shape, location, temperature level, and duration). Since the control is based only on voxels inside the target volume, it does not prevent against any near or far field issues, such as poor coupling or bone structures that might cause unwanted local heating, especially for larger target volumes using an increased total acoustical energy.

The control of the stability of the temperature SD used in the nonheated region was an efficient way to prevent against adverse events such as tissue displacement (which was the case for the last rabbit experiment *in vivo*, which was automatically interrupted), susceptibility artifacts, or electromagnetic interferences between the MRI and other devices such as the HIFU system. In addition, the safety could be improved by monitoring the temperature level of voxels adjacent to the target volume.

The heating procedure required only a few minutes to produce a lethal dose for 287 target voxels of  $1 \times 1 \times 4 \text{ mm}^3$  (more than 1 ml). The maximum number of voxels under control was limited by the practical capability of focal point steering and by the MRI resolution, providing a sufficient SNR. In addition, this fast volumetric heating procedure may induce significant stress on the transducer when no interleaved cool-down periods are used. Since the total energy emission increases with the treated volume, users should be careful to avoid transducer overheating. This technical consideration may currently constitute a limitation in the treatment duration.

A shorter treatment duration minimizes the diffusion effect and the total energy deposited. It also reduces the risk that motion will occur during the heating duration. Phased-array transducers offer a very fast displacement of the focal point with 15 positions updated per second (for our in-house-designed HIFU system). Therefore, this volumetric heating temperature control may also be combined with motion tracking of the target region, as recently demonstrated (22).

## ACKNOWLEDGMENTS

We thank the Imasonic SA, TDM SA, RCDC SA, and TSR SA companies for technological support.

## REFERENCES

1. Lele PP. Production of deep focal lesions by focused ultrasound—current status. *Ultrasonics* 1967;5:105–112.
2. Hynynen K, McDannold N, Clement G, Jolesz FA, Zadicario E, Killiany R, Moore T, Rosen D. Pre-clinical testing of a phased array ultrasound system for MRI-guided noninvasive surgery of the brain—a primate study. *Eur J Radiol* 2006;59:149–56.
3. Hynynen K, Damianou C, Darkazanli A, Unger E, Schenck JF. The feasibility of using MRI to monitor and guide noninvasive ultrasound surgery. *Ultrasound Med Biol* 1993;19:91–92.
4. Hindman J. Proton resonance shift of water in the gas and liquid states. *J Chem Phys* 1966;44:4582–4592.
5. Denis de Senneville B, Quesson B, Moonen CTW. Magnetic resonance temperature imaging. *Int J Hypertherm* 2005;21:515–531.
6. Tempny CM, Stewart EA, McDannold N, Quade BJ, Jolesz FA, Hynynen K. MR imaging-guided focused ultrasound surgery of uterine leiomyomas: a feasibility study. *Radiology* 2003;226:897–905.
7. Arora D, Cooley D, Perry T, Skliar M, Roemer RB. Direct thermal dose control of constrained focused ultrasound treatments: phantom and in-vivo evaluation. *Phys Med Biol* 2005;50:1919–35.
8. Arora D, Minor MA, Skliar M, Roemer RB. Control of thermal therapies with moving power deposition field. *Phys Med Biol* 2006;51:1201–1219.
9. Salomir R, Vimeux F, de Zwart J, Grenier N, Moonen CTW. Hyperthermia by MR-guided focused ultrasound: accurate temperature control based on fast MRI and a physical model of local energy deposition and heat conduction. *Magn Reson Med* 2000;43:342–347.
10. Mougenot C, Salomir R, Palussière J, Grenier N, Moonen CTW. Automatic spatial and temporal temperature control for MR-guided focused ultrasound using fast 3D MR thermometry and multispiral trajectory of the focal point. *Magn Reson Med* 2004;52:1005–1015.
11. Huttunen JM, Huttunen T, Malinen M, Kaipio JP. Determination of heterogeneous thermal parameters using ultrasound induced heating and MR thermal mapping. *Phys Med Biol* 2006;51:1011–1032.
12. Pennes HH. Analysis of tissue and arterial blood temperatures in the resting human forearm. *J Appl Physiol* 1948;1:93–122.
13. Gavrilov LR, Hand WH. A theoretical assessment of the relative performance of spherical phased arrays for ultrasound surgery. *IEEE Trans Ultrasonics* 2000;47:125–139.
14. Quesson B, de Zwart JA, Moonen CT. Magnetic resonance temperature imaging for guidance of thermotherapy. *J Magn Reson Imaging* 2000;12:525–533.
15. McDannold N, Jolesz FA. Magnetic resonance image-guided thermal ablations. *Top Magn Reson Imaging* 2000;11:191–202.
16. Lele PP. Induction of deep, local hyperthermia by ultrasound and electromagnetic fields: problems and choices. *Radiat Environ Biophys* 1980;17:205–217.
17. Sokka SD, King R, Hynynen K. MRI-guided gas bubble enhanced ultrasound heating in in vivo rabbit thigh. *Phys Med Biol* 2003;48:223–241.
18. Moonen CTW, Mougenot C. MRI-guided focused ultrasound, apparatus for novel treatment of breast cancer. Berlin: Springer; 2006. p 183–2000.
19. El-Sharkawy AM, Schar M, Bottomley PA, Atalar E. Monitoring and correcting spatio-temporal variations of the MR scanner's static magnetic field. *MAGMA* 2006;19:223–236.
20. Meshorer A, Prionas SD, Fajardo LF, Meyer JL, Hahn GM, Martinez AA. The effects of hyperthermia on normal mesenchymal tissues. Application of a histologic grading system. *Arch Pathol Lab Med* 1983;107:328–334.
21. Sapareto SA, Dewey CW. Thermal dose determination in cancer therapy. *Int J Radiat Oncol Biol Phys* 1984;10:787–800.
22. de Senneville BD, Mougenot C, Moonen CT. Real-time adaptive methods for treatment of mobile organs by MRI-controlled high-intensity focused ultrasound. *Magn Reson Med* 2007;57:319–330.